Photoacoustics 28 (2022) 100390

Contents lists available at ScienceDirect

Photoacoustics

journal homepage: www.elsevier.com/locate/pacs

Pixel-wise reconstruction of tissue absorption coefficients in photoacoustic tomography using a non-segmentation iterative method

Shuangyang Zhang [a,b,c,1], Jiaming Liu [a,b,c,1], Zhichao Liang [a,b,c], Jia Ge [a,b,c], Yanqiu Feng [a,b,c,*], Wufan Chen [a,b,c,*], Li Qi [a,b,c,*]

[a] School of Biomedical Engineering, Southern Medical University, Guangzhou, Guangdong, China
[b] Guangdong Provincial Key Laboratory of Medical Image Processing, Southern Medical University, Guangzhou, Guangdong, China
[c] Guangdong Province Engineering Laboratory for Medical Imaging and Diagnostic Technology, Southern Medical University, Guangzhou, Guangdong, China

ARTICLE INFO

Keywords:
Photoacoustic Tomography
Quantitative imaging
Absorption coefficient
Endogenous and exogenous agents

ABSTRACT

In Photoacoustic Tomography (PAT), the acquired image represents a light energy deposition map of the imaging object. For quantitative imaging, the PAT image is converted into an absorption coefficient (μ_a) map by dividing the light fluence (LF). Previous methods usually assume a uniform tissue μ_a distribution, and consequently degrade the LF correction results. Here, we propose a simple method to reconstruct the pixel-wise μ_a map. Our method is based on a non-segmentation-based iterative algorithm, which alternately optimizes the LF distribution and the μ_a map. Using simulation data, as well as phantom and animal data, we implemented our algorithm and compared it to segmentation-based correction methods. The results show that our method can obtain accurate estimation of the LF distribution and therefore improve the image quality and feature visibility of the μ_a map. Our method may facilitate efficient calculation of the concentration distributions of endogenous and exogenous agents in vivo.

1. Introduction

Photoacoustic tomography (PAT) or optoacoustic tomography (OAT), as a hybrid biomedical imaging modality, is able to acquire the instant light energy deposition inside an imaged object by detecting and processing the ultrasonic signal generated by laser illumination [1–4]. Utilizing multiple wavelength excitation, multispectral PAT can distinguish the distribution of endogenous tissue absorbers, such as oxyhemoglobin (HbO_2) and de-oxyhemoglobin (Hb), and exogenous optical probes such as the FDA-approved Indocyanine Green (ICG) based on their specific absorption spectrum [5]. Benefiting from high imaging speed, good detection sensitivity and centimeter-scale imaging depth, PAT has been used in various preclinical researches and clinical trials [6–10].

Within a given voxel, the PAT image intensity is proportional to the absorbed light energy density, which is the product of the light fluence (LF) arriving at that voxel and the absorption coefficient (μ_a) of the enclosed absorbers [11]. Deriving the distribution of the estimated μ_a by removing the LF distribution can help obtain a quantitative concentration map of the absorbers [12]. Although there are currently some methods that can achieve quantitative blood oxygen saturation (sO_2) measurement without LF correction (e.g., acoustic-spectrum-based methods [13,14] and the absorption-saturation-based method [15]), estimating and correcting for the LF can further improve the accuracy of the measurement. Indeed, the true LF distribution of the imaged object is very difficult to measure, and thus is usually approximated by using light transport models. These models include the radiative transfer equation (RTE) [16,17], diffusion equation (DE, a simplified form of the RTE) [18,19], and numerical simulations based on the Monte Carlo method [20,21]. Despite this, the estimation of the LF distribution relies on the prior information of the absorption distribution, which poses challenges for quantitative PAT imaging.

Previous studies for quantitative PAT imaging can be divided into experimental methods and simulation-based methods [11]. Experimental methods aim to measure the absorption and scattering of light within samples using external gauging devices. For example, Bauer et al. proposed the use of diffuse optical tomography to measure the surface scattered light and then used it to infer the LF distribution within the

* Corresponding authors at: School of Biomedical Engineering, Southern Medical University, Guangzhou, Guangdong, China.
E-mail addresses: foree@smu.edu.cn (Y. Feng), chenwf@smu.edu.cn (W. Chen), qili@smu.edu.cn (L. Qi).
[1] These authors contributed equally to this work

https://doi.org/10.1016/j.pacs.2022.100390
Received 24 April 2022; Received in revised form 30 June 2022; Accepted 14 August 2022
Available online 17 August 2022

sample [22]. Steenbergen et al. used acousto-optic tomography to measure the LF distribution [23]. These methods required additional instruments and thus their application in PAT was limited. Simulation-based methods estimate the LF distribution based on the acquired PAT image or combined with co-registered images of other modalities, such as ultrasound (US) [24] and magnetic resonance imaging (MRI) [18]. Representative simulation-based techniques include the direct correction method [25], fixed-point iteration method [12], and model-based methods [26–28]. Banerjee et al. proposed the direct correction method to obtain the LF distribution by assuming that the reduced scattering coefficient ($\mu_s^{'}$) is known a priori and thus the diffusion coefficient $\kappa = 1/3\mu_s^{'}$ [25]. Cox et al. proposed the fixed-point iteration method to obtain μ_a map without making linear assumptions [12], but the method diverges quickly if the prior knowledge of the scattering distribution is incorrect [11,29]. The model-based minimization methods aim to minimize a functional quantifying the difference between the model output and the measured data by adjusting the μ_a distribution. For example, Jiang et al. applied the Gauss-Newton method to minimize the objective function and tackle the inversion of μ_a [26]. Cox et al. achieved greater computational efficiency by accelerating the calculation of the functional gradient vector with an adjoint model, but at the cost of requiring more iterations to converge [27,28]. Compared to other techniques, the model-based methods usually yield better results.

To alleviate the computational complexity, segmentation-based methods have been proposed. Such methods generally assume that the imaging object has the same optical parameters, and require segmentation of the object contours. After assigning initial optical parameters to the segmented image, LF estimation can be performed using light transport models. Based on their solution algorithms, the simulation-based methods can be divided into two categories: segmentation-based direct correction (SBDC) methods, and segmentation-based iterative correction (SBIC) methods. The SBDC methods, such as Ref [30], directly obtained the μ_a map by dividing the PAT image by the obtained LF map [Fig. 1(c)]. However, these methods require manual selection of ideal initial optical parameters for each segmented region. The SBIC methods first segment the object contours in the PAT image and assume a uniform μ_a value [Fig. 1(d)], and then iteratively estimates the LF distribution by minimizing the error between the acquired PAT image and an estimated PAT image. To ease the manual intervention requirement of the simulation-based methods, Liang et al. proposed an automatic segmentation algorithm to obtain the animal contours for LF estimation [31]. Brochu et al. proposed organ-level segmentation to improve the accuracy of LF estimation [32]. However, the poor soft-tissue contrast of PAT images makes precise organ segmentation challenging. Recently, Pattyn et al. proposed to use co-registered US images to segment phantom images [24]. Zhang et al. proposed to use co-registered MR images to obtain a more refined segmentation of animal organs to improve LF estimation [33]. These attempts focused on improving segmentation efficiency and accuracy. However, they all started from the assumption of a uniform μ_a distribution within a region (or organ), whereas tissue μ_a values are actually spatially inhomogeneous. This inaccurate assumption leads to errors in the estimation of μ_a distribution. At present, there is still a lack of simple and convenient method that can accurately reconstruct a pixel-wise μ_a map for PAT.

To meet the above challenges, we propose a simple, non-segmentation method to directly reconstruct the spatially varying μ_a distribution. We treat the tissue μ_a distribution as a pixel-wise spatially varying map and thus avoid the need for segmentation. Unlike previous optimization schemes for numerical models [16,34], our method does not need to calculate Hessian matrices or gradient vectors of the objective function, but instead employs a two-step iterative algorithm to alternately optimize the LF distribution and the μ_a map [Fig. 1(e)]. We tested our method in numerical simulation experiments, tissue-mimicking phantom experiments, and live animal experiments. The results show that, compared with the SBDC and SBIC methods, our method reconstructs an accurate μ_a map that removes the signal inhomogeneity induced by light fluence attenuation. Based on the obtained μ_a map, spectral unmixing experiments on in vivo animals further show enhanced visualization of endogenous and exogenous contrast agents in deep tissues. This simple and convenient μ_a reconstruction method has the potential for the efficient quantification of absorber concentration in future PAT applications.

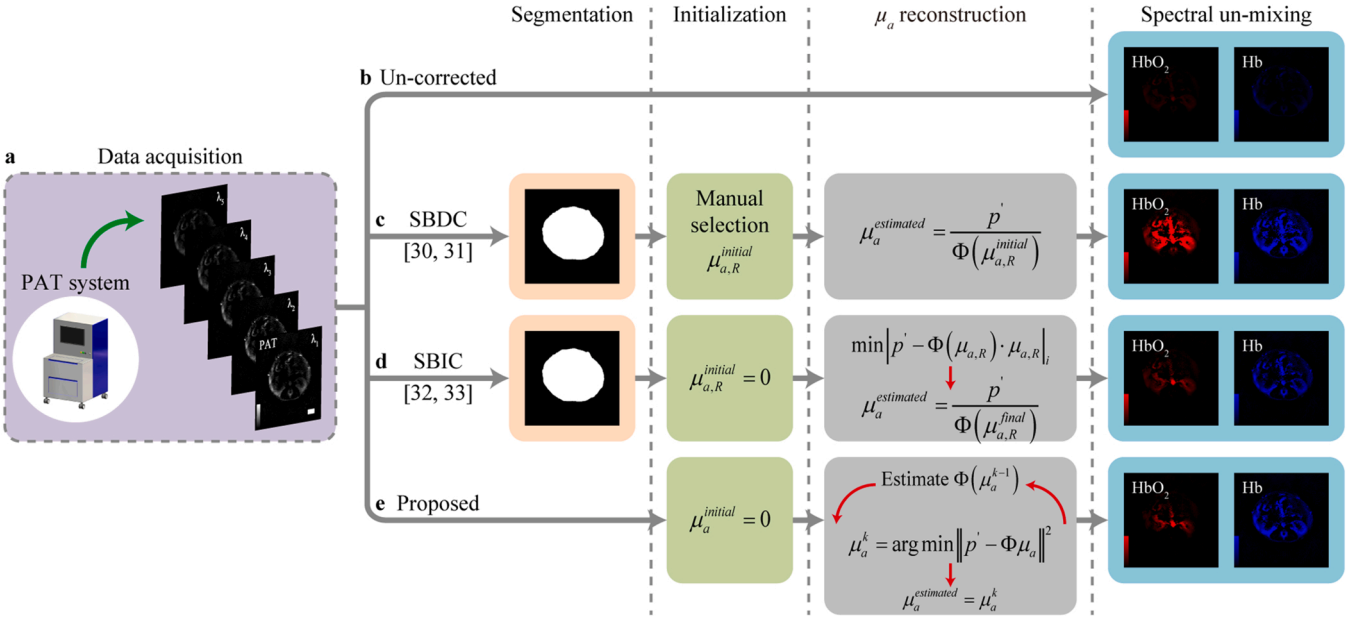

Fig. 1. Schematic diagram of quantitative μ_a reconstruction in PAT. (a) Data acquisition: multispectral PAT images are acquired. (b) Un-corrected: un-corrected PAT images. (c) SBDC: segmentation-based direct correction. (d) SBIC: segmentation-based iterative correction. (e) Proposed: our proposed non-segmentation iterative algorithm. Segmentation: prior images for SBDC and SBIC methods. Initialization: initialization of μ_a values. μ_a reconstruction: Schematic diagram of different methods to obtain μ_a images. The fluence forward model is employed to estimate LF distribution. Spectral un-mixing: identify the distribution of endogenous absorbers (HbO_2, Hb) from the background. Scale bar, 3 mm.

2. Method

2.1. The imaging model of PAT

The PAT images are formed by reconstructing the original point source of the ultrasonic waves generated by absorbing the laser pulse, and the pixel value $p(\vec{r})$ in the image can be expressed as:

$$p(\vec{r}) = \Gamma\mu_a(\vec{r})\Phi\left[(\vec{r}), \mu_a(\vec{r}), \mu_s'(\vec{r})\right], \tag{1}$$

where Γ denotes the thermo-elastic Grüneisen parameter, $\mu_a(\vec{r})$ and $\mu_s'(\vec{r})$ denote the absorption and reduced scattering coefficients, Φ denotes the LF within a voxel at the position $\vec{r}$. In the beginning, we make an assumption that p has been reconstructed from the acoustic measurements accurately and with negligible structural distortion [35–39]. In biological soft tissue, the thermo-elastic Grüneisen parameter has a small variation so that it is assumed to be constant [32]. Then, the distribution of absorbed energy p' is obtained by eliminating the constant terms from p. Finally, the PAT image p' can be expressed as the product of the LF distribution Φ and the μ_a map:

$$p' = \Phi(\mu_a, \mu_s')\cdot\mu_a, \tag{2}$$

However, solution of μ_a from Eq. (2) is considered difficult because the LF matrix Φ depends on both μ_a and μ_s'. μ_s' is the reduced scattering coefficient, which can be calculated by $\mu_s' = \mu_s(1-g)$, where μ_s represents the scattering coefficient, g represents the scattering anisotropy. Thus, it is often assumed that μ_s' is known [12,32,40,41]. Accordingly, the imaging model can be expressed as:

$$p' = \Phi(\mu_a)\cdot\mu_a = H(\mu_a), \tag{3}$$

where $H(\bullet)$ represents the mapping function that relates the μ_a map to the PAT image p'. The objective of quantitative PAT imaging is then to formulate an inverse mapping $H^{-1}(\cdot)$ to obtain μ_a, which can be expressed as:

$$\mu_a = H^{-1}(p'). \tag{4}$$

2.2. The segmentation-based LF correction methods

Since organ-level segmentation is difficult to achieve in animal experiments, all the segmentation-based methods involved in this paper segment the object contours and assume a uniform optical parameter within the whole imaging object. The SBDC method assumes a uniform distribution of μ_a within the imaged object [Fig. 1(c)], and the LF map can be estimated by manually selecting the initial value $\mu_{a,R}^{initial}$ and then obtain the estimated μ_a ($\mu_a^{estimated}$) image [30,31]. It can be expressed as [Fig. 1(c)]:

$$\mu_a^{estimated} = \frac{p'}{\Phi\left(\mu_{a,R}^{initial}\right)}. \tag{5}$$

The SBIC method first segments the object contours in the PAT image and assumes a uniform μ_a value [Fig. 1(d)], and then iteratively calculate the μ_a value to minimize the error between the product $\Phi(\mu_{a,R})\cdot\mu_{a,R}$ and the un-corrected PAT image [32,33]. It can be expressed as [Fig. 1(d)]:

$$\mu_{a,R}^{final} = arg\min\left|p' - \Phi(\mu_{a,R})\cdot\mu_{a,R}\right|_i. \tag{6}$$

The LF map $\Phi\left(\mu_{a,R}^{final}\right)$ can be estimated using the final μ_a value $\mu_{a,R}^{final}$. Then, by dividing the un-corrected PAT image by the LF map, we can obtain the $\mu_a^{estimated}$ map:

$$\mu_a^{estimated} = \frac{p'}{\Phi\left(\mu_{a,R}^{final}\right)}. \tag{7}$$

2.3. The proposed iterative algorithm

With Eq. (3), the imaging model can be represented as a nonlinear model:

$$p' = \Phi(\mu_a)\mu_a, \tag{8}$$

where p' and μ_a are in vector representation, Φ is in sparse matrix representation. We can then formulate the solution of μ_a as a least square optimization problem:

$$\widehat{\mu}_a = arg\min\|p' - \Phi(\mu_a)\mu_a\|^2. \tag{9}$$

The direct solution of the above objective function is difficult because the LF matrix Φ depends on μ_a. However, if we can solve Φ and μ_a one by one and then alternately update each of them, we might be able to reach their optimized solutions. Based on this idea, a two-step iterative optimization method based on gradient descent was developed [Fig. 1(e)] to solve the nonlinear model in Eq. (9). To start with, the μ_a map is initialized as 0. During each iteration, we first use the updated μ_a map to obtain the LF matrix Φ. Then, the objective function is converted into a linear model, from which the μ_a map can be updated by gradient descent algorithm. These two steps are repeated until convergence. The detailed steps of our method are summarized in Algorithm 1.

Table
Algorithm 1 Two-Step Iterative Algorithm

Input: $\mu_a^{(0)} = 0$, μ_s', k, $Iter$ max, ε.

Repeat

1. Update Φ^k using the diffusion equation (DE) with μ_a^{k-1}, μ_s'.
2. Update μ_a^k by solving $\mu_a^k = \arg\min\left\|p' - \Phi^k\mu_a\right\|^2$ with the constraint that $\mu_a \geq 0$.
3. Calculate the error: $err \leftarrow norm\left(p' - \Phi^k\mu_a^k\right)$.
4. Update the iterations: $k \leftarrow k + 1$.

Until convergence where $k > Iter$ max or $err < \varepsilon$.

Output: μ_a^k.

In the above two-step iterative algorithm, the LF distribution was modeled in the 2D plane by the DE, which was performed in MATLAB (The MathWorks, Inc., USA) using the open-source finite-element-based LF simulation software Toast++ toolbox [42]. During the optical transport modeling process, the background medium is set as water and the μ_a map is initialized as 0 [Fig. 1(e)]. For all experiments, the *Iter* max is set to 30 and ε is set to 10^{-12}. The average computation time for a single-slice image is 92.49 s

Compared to previous SBDC and SBIC methods, our two-step iterative algorithm solves for a pixel-wise μ_a map rather than a region-wise map. It does not require manual segmentation of the sample as well as initialization with a coarse μ_a estimation, and therefore avoids subjective variation of the observers. Also, allowing the μ_a map to vary for each image pixel, the objective function of Eq. (9) should converge to a more ideal solution.

2.4. Spectral un-mixing

The reconstructed μ_a image is a combination of various endogenous and exogenous absorbers. There is a linear relationship between the image $\mu_a(\lambda)$ and the value $\mu_a^i(\lambda)$ of the identified chromophore i:

$$\mu_a(\lambda) = \sum_i \mu_a^i(\lambda) = \sum_i c_i \varepsilon_i(\lambda), \tag{10}$$

where, c_i is the concentration of chromophore i and $\varepsilon_i(\lambda)$ is the molar extinction coefficient at λ wavelength. In multispectral PAT, the core idea of spectral separation is to decompose the distribution of each absorber by identifying the specific absorption curve of each absorber. In this paper, we choose the most commonly used linear un-mixing method to calculate the distribution of HbO_2, Hb and ICG [43]. After obtaining the concentrations of HbO_2 (c_{HbO_2}) and Hb (c_{Hb}), sO_2 can be computed as:

$$sO_2 = \frac{c_{HbO_2}}{c_{HbO_2} + c_{Hb}}. \tag{11}$$

2.5. Experimental setups

2.5.1. PAT imaging

A commercial small animal multispectral optoacoustic tomography system (MSOT inVision128, iThera Medical, Germany) was employed for imaging. Fig. 2(a) shows a diagram of the imaging chamber of the MSOT system. Pulsed laser (670–960 nm tunable) with pulse width < 10 ns, repetition rate of 10 Hz, and a peak pulse energy of 60 mJ at 760 nm excite the sample through a ten-arm fiber bundle, which provides homogeneous, 360-degree illumination of approximately 8 mm width over the surface of the imaged object. The generated ultrasonic waves are detected by ring-array ultrasound transducer with a center frequency of 5 MHz (60 % bandwidth). The ring-array transducer has 128 elements in the 270-degrees range [44]. The array radius is 40.5 mm. Fig. 2(b) shows the schematic of the ring-array ultrasound transducer setting. PAT images are averaged with signals from 10 frames per wavelength. The ultrasound time-series signals are then reconstructed into 2D PAT images using a model-based iterative reconstruction algorithm [37] with a field of view 30 mm × 30 mm and matrix 300 × 300. Negative values of the reconstructed image are set to zero on the basis that the absorbed energy cannot be negative.

2.5.2. Simulation experiments

In the simulation experiments, we first designed a mouse example to compare the performance between our proposed method and two other comparing methods. Similar to Ref [12,36], our simulation experiments only incorporate the optical inversion problem that needs to be addressed in this paper, but not the acoustic inversion. We employed a mouse organ model to generate the simulation images, as shown in

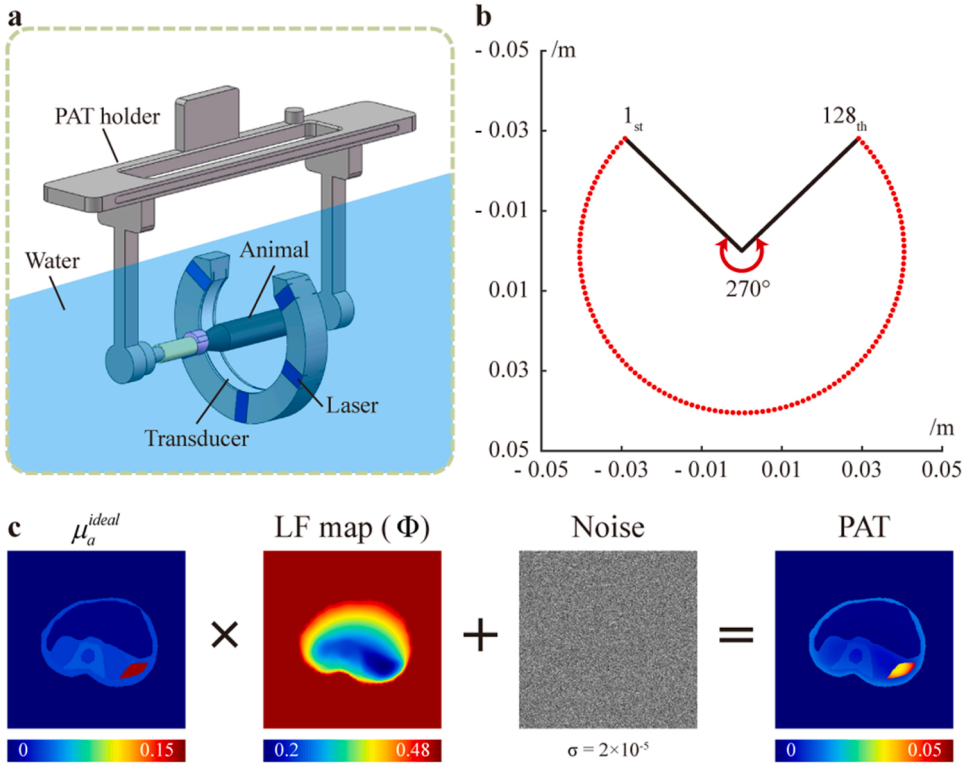

Fig. 2. (a) Diagram of the PAT system. (b) Schematic of the ring-array ultrasound transducer setting. (c) The process of obtaining the un-corrected PAT images used in the simulation experiments. μ_a^{ideal}: ideal μ_a image. LF map (Φ): estimated light fluence distribution using μ_a^{ideal} image. Noise: noise with a mean of 0 and a standard deviation of 2×10^{-5} was added to the un-corrected PAT image. PAT: un-corrected PAT image.

Fig. 2(c). The μ_a value of each organ can be calculated by referring to Ref [45]:

$$\mu_a(\lambda) = S\left(x\mu_{aHbO_2} + (1-x)\mu_{aHb}\right), \tag{12}$$

where x was sO_2, S was a scaling factor relative to whole blood. The values of S and x for different organs are listed in Supplementary Table 1. The μ_a values of HbO_2 and Hb at different wavelengths were determined by referring to Ref [36]. These values are listed in Supplementary Table 2. The μ_s' value of each organ was calculated by referring to Ref [45]. These values are listed in Supplementary Table 3. Next, we designed a simulation example that includes vascular network with varying diameters (minimum: 200 μm). The vascular network contains arteries and veins, and the sO_2 values of the arteries and veins are set to 100 % and 75 %, respectively. The scattering coefficient μ_s and scattering anisotropy g values of HbO_2 and Hb at different wavelengths were also derived from Ref [36]. The calculated μ_s' values are listed in Supplementary Table 2.

Fig. 2(c) presents the process of obtaining the un-corrected PAT images. We used Toast+ + software to obtain the LF distribution Φ. As a result, the absorbed energy is proportional to the product of the μ_a and the LF intensity within a given voxel. We multiplied the ideal μ_a (μ_a^{ideal}) images by the LF images Φ to obtain the un-corrected PAT images. To further approximate the un-corrected PAT image, we added noise with a mean of 0 and a standard deviation of 2×10^{-5} to the un-corrected PAT images. According to the above procedure, multispectral PAT images were acquired at five different illumination wavelengths: 700, 730, 760, 800 and 850 nm. In the later μ_a reconstruction procedure, the μ_a map was initialized to 0 and the μ_s' values were fixed to the ideal value. Then, a linear spectral un-mixing algorithm was performed to decompose the distribution of the absorbers (HbO_2 and Hb) from the μ_a^{ideal}, PAT and $\mu_a^{estimated}$ images. Lastly, a high-pass filter was used to filter out the HbO_2 and Hb signals in the background.

2.5.3. Phantom experiments

We constructed a tissue-mimicking phantom containing rod-shaped inclusions to further evaluate our proposed method. The standard and method for making the phantom are based on Ref [33,46]. The background of the phantom was an agar solution mixed with 0.5% Intralipid designed to enhance scattering. Before its solidification, three 3D printed rod molds were inserted into the background solution. After the solution cooled and solidified, the molds were pulled out and three rod-shaped absorbers containing agar solution mixed with 0.5 % Intralipid and 0.02 % Chinese ink were inserted. Referring to Ref [46], the μ_a and μ_s' values were determined to be 0.12 mm^{-1}, 0.5 mm^{-1} for the absorbers and 0.006 mm^{-1}, 0.5 mm^{-1} for the background solution at 700 nm, respectively. The diameter of the phantom is 20 mm and the diameter of each inclusion is 3 mm. In addition, we made a phantom containing three absorbers with different μ_a values. The μ_a values of the three absorbers are 0.05 mm^{-1}, 0.1 mm^{-1}, and 0.15 mm^{-1}, respectively. PAT images at 700 nm were acquired and the speed of sound was set to 1500 m/s. In the later μ_a reconstruction procedure, the μ_a map was initialized to 0 and the μ_s' value was fixed to 0.5 mm^{-1}.

2.5.4. Animal experiments

In in vivo animal imaging experiments, four healthy nude mice (female, 8 weeks, Southern Medical University, Guangzhou, China) were used. Animals were kept in ventilated cages inside a temperature-controlled room, under a 12-h dark/light cycle. To reduce abdominal peristalsis artifacts caused by food digestion and to prevent the mice from excreting and polluting the imaging environment during PAT imaging, the nude mice have fasted for 8 h before imaging. All animal experiments were approved by the local Animal Ethics Committee of Southern Medical University and were performed under current guidelines.

To reduce the image artifacts caused by respiratory movements, medical oxygen mixed with 1 % isoflurane (RWD Life Science Co., Ltd, China) was transmitted to the breathing mask, so that the respiratory rate of nude mice was maintained at 15–20 breath/min. For PAT imaging without contrast enhancement, multispectral PAT images of kidney, liver, head, neck and other positions were acquired at five different illumination wavelengths: 700, 730, 760, 800 and 850 nm. For contrast-enhanced PAT imaging, an insulin injection needle was embedded into the tail vein in advance, and was connected to a long Polyethylene Tubing 10 (PE 10) that enabled probe injection (ICG) from outside the imaging chamber. Multispectral PAT images of kidney, liver and other positions were acquired at seven different illumination wavelengths: 740, 760, 780, 800, 820, 840 and 860 nm. For the reconstruction, the speed of sound was set to 1536 m/s. In the later μ_a reconstruction procedure, the μ_a map was initialized to 0 and the μ_s' value was fixed by referring to Supplementary Table 4. Finally, the linear un-mixing algorithm was used to calculate the distribution of HbO_2, Hb.

2.6. Image quality metrics

The quantitative performance metrics used to evaluate the performance of the correction algorithm include L2-norm PAT image error (Err) and the sum of squares error of the μ_a images (SSE). Here, the product of the μ_a map and the LF distribution Φ is defined as the estimated PAT image (ePAT) to approximate the un-corrected PAT image.

The L2-norm PAT image error is a metric to evaluate the convergence performance of the correction algorithm by calculating the error between the un-corrected PAT image and the ePAT image as:

$$\mathrm{Err} = \left(\sum_{j=1}^{N} \left(PAT_j - ePAT_j\right)^2 \right)^{\frac{1}{2}} \tag{13}$$

where, PAT is the un-corrected PAT image and ePAT is the estimated PAT image. N is the total pixel number of the image.

The SSE is used to evaluate the error between the μ_a^{ideal} image and the reconstructed $\mu_a^{estimated}$ images in the simulation experiments. It is defined as:

$$\mathrm{SSE} = \sum_{j=1}^{N} \left(\mu_a^{ideal} j - \mu_{a,j}^{estimated} j\right)^2 \tag{14}$$

where, μ_a^{ideal} and $\mu_a^{estimated}$ are the ideal μ_a image and the reconstructed μ_a image, respectively.

3. Results

3.1. Simulation Results

The results of the simulation experiment are shown in Fig. 3. In the μ_a^{ideal} images, the same concentration of absorber has a uniform μ_a signal intensity at each organ, as shown in Fig. 3(a). However, due to the attenuation of laser energy in the transmission process, the PAT signal weakens with the increase of imaging depth, as shown in Fig. 3(b). The prior images of SBDC and SBIC methods are shown in Fig. 3(c), which is generated by manually segmenting the object contours from the PAT image. The LF distribution maps estimated using different methods are shown in Fig. 3(d). The ePAT images are shown in Fig. 3(e) and the reconstructed $\mu_a^{estimated}$ images are shown in Fig. 3(f). In the SBDC method, we choose 0.05832 mm^{-1} (average of all organs) as the μ_a value. In the SBIC method, the optimal μ_a value calculated by iteration is 0.01911 mm^{-1}.

As can be seen from the result of the SBDC method, the $\mu_a^{estimated}$ image shows excessive enhancement of central features (such as muscles and kidneys) [Fig. 3(f)]. In the $\mu_a^{estimated}$ image obtained from the SBIC

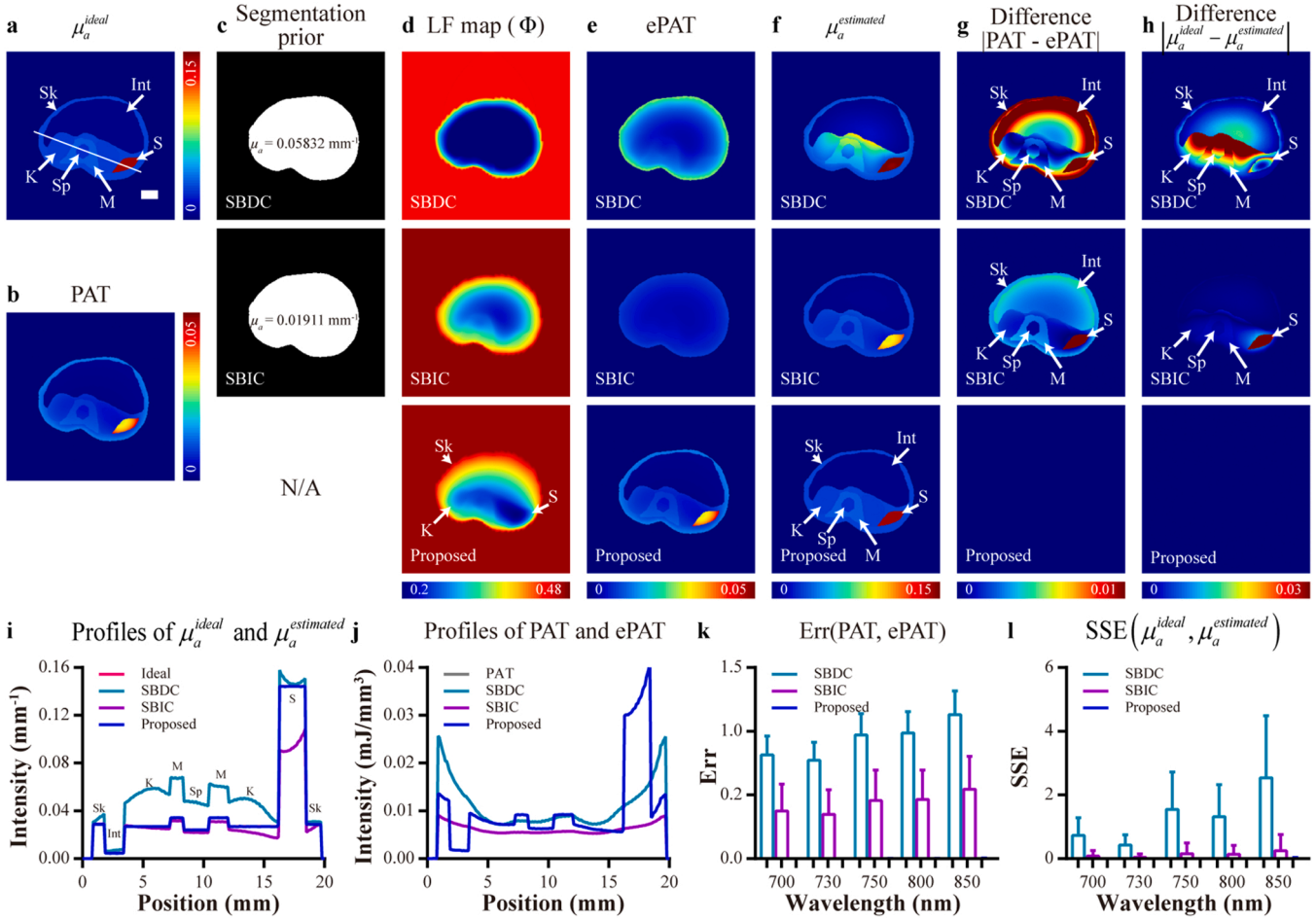

Fig. 3. Simulation results: (a) μ_a^{ideal}: ideal μ_a distribution image at 850 nm. (b) PAT: un-corrected PAT image at 850 nm obtained by multiplying the μ_a^{ideal} image with the LF map and adding ~40 dB of noise. (c) Segmentation prior: segmentation results for SBDC and SBIC methods. (d) LF map (Φ): light fluence distribution map estimated using different methods. (e) ePAT: estimated PAT image derived by using different methods. (f) $\mu_a^{estimated}$: μ_a image solved by different methods. (g) Difference: the difference images between PAT and ePAT images. (h) Difference: the difference images between μ_a^{ideal} and $\mu_a^{estimated}$ images. (i) Profiles of μ_a^{ideal} and $\mu_a^{estimated}$ images drawn along the white solid line in (a). (j) Profiles of PAT and ePAT images drawn along the white solid line in (a). (k) The Err values between PAT and ePAT images for all positions. (l) The SSE values between μ_a^{ideal} and $\mu_a^{estimated}$ images for all positions. Description of markers: Sk: skin; Int: intestines; K: kidney; Sp: spine; M: muscle; S: spleen. Scale bar, 3 mm.

method, the degree of enhancement is appropriate [Fig. 3(f)], but the signal within the same organ of the $\mu_a^{estimated}$ image is still inhomogeneous (e.g., spleen). The $\mu_a^{estimated}$ image obtained by our proposed method eliminates the phenomenon of a lower signal at larger depths, and the signal in each organ has reached an even distribution [Fig. 3(f)]. The reason for this improvement can be found in the LF map and the estimated PAT images shown in Fig. 3(d) and Fig. 3(e) respectively. The LF map estimated by our method has a rapid decay in the spleen, which is caused by the higher μ_a value. However, the LF map obtained by SBDC and SBIC methods can not reflect this phenomenon. The ePAT image obtained by the SBIC method does not approximate the un-corrected PAT image because of the assumption of uniform μ_a. In contrast, using our method, the ePAT image is very close to the un-corrected PAT image. This proves the accuracy of our proposed iterative algorithm for solving the nonlinear model.

Next, we have calculated the difference between PAT and ePAT, μ_a^{ideal} and $\mu_a^{estimated}$ images. The results are shown in Fig. 3(g, h). It can be observed that the difference of the SBDC method is the largest, whereas the SBIC method only has a greater difference at organs with higher μ_a values (e.g., spleen), and the difference gradually increases with increasing imaging depth. In contrast, the difference in our proposed method is so small that it cannot be observed.

For further comparison, Fig. 3(i, j) shows the image profiles of the μ_a^{ideal}, $\mu_a^{estimated}$, PAT and ePAT. The position of the profiles is along the white solid line in Fig. 3(a). The profiles of the $\mu_a^{estimated}$ image show that there are errors in the SBDC and SBIC methods compared to the μ_a^{ideal} image. These problems have been addressed by the $\mu_a^{estimated}$ image obtained by our proposed method, as evidenced by the highly overlapping profiles between the μ_a^{ideal} and reconstructed $\mu_a^{estimated}$ image [Fig. 3(i)]. Fig. 3(j) also shows a high degree of overlap between the un-corrected PAT and ePAT images obtained by our proposed method, which demonstrates the high reliability of our model solutions. Moreover, the Err between the entire PAT and ePAT images, the SSE between the entire μ_a^{ideal} and $\mu_a^{estimated}$ images for all positions are shown in Fig. 3(k, l). For both Err and SSE, our proposed method possesses the smallest value (two orders of magnitude smaller than the SBIC method).

Next, we acquired HbO_2 and Hb distribution images and further calculated the sO_2, as shown in Fig. 4(a-e). As can be seen from the un-corrected results, the light energy attenuation process affects the spectral un-mixing, resulting in the concentration decrease with the increase of depth in the HbO_2 and Hb images [Fig. 4(b)]. This further leads to varying sO_2 values within the same organ (contrary to the ideal value). Greater error is observed at the organs with a higher absorption coefficient (e.g., spleen) and deeper spatial distribution (e.g. kidney) [Fig. 4

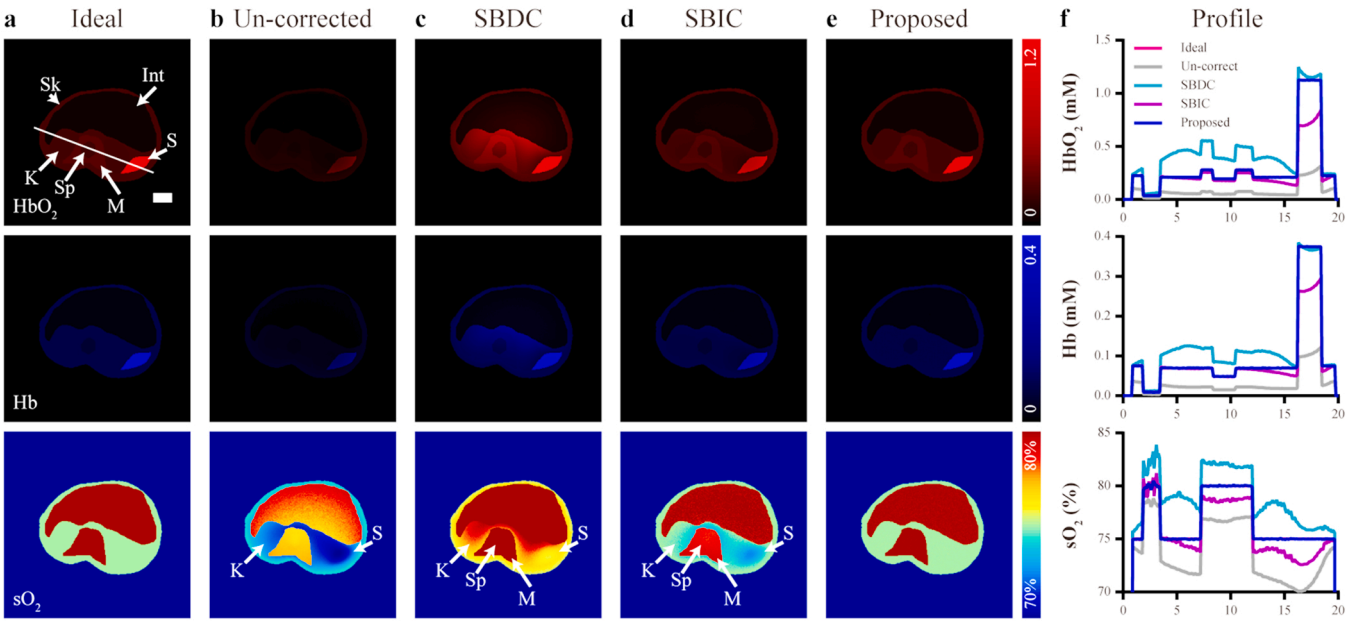

Fig. 4. Spectral un-mixing results of simulation experiment: (a-e) The concentration distribution (HbO_2, Hb) and sO_2 images obtained by spectral un-mixing from μ_a^{ideal}, un-corrected PAT and $\mu_a^{estimated}$ images. (f) Profiles of HbO_2, Hb and sO_2 drawn along the white solid line in (a). Description of markers: Sk: skin; Int: intestines; K: kidney; Sp: spine; M: muscle; S: spleen. Scale bar, 3 mm.

(b)]. The SBDC and SBIC methods enhance the concentrations of HbO_2 and Hb in the depth of the image [Fig. 4(c, d)], but failed to accurately compensate for the LF in the kidneys, muscle, spine and spleen. There are still quantitative errors in the sO_2 values of these regions. Our proposed method brings the concentrations of HbO_2 and Hb in each organ to a uniform distribution, and the sO_2 values are consistent with the ideal values [Fig. 4(e)].

The image profiles of HbO_2, Hb and sO_2 are illustrated in Fig. 4(f). The position of the profiles is along the white solid line in Fig. 4(a). The HbO_2, Hb and sO_2 of un-corrected are lower than ideal values, and they are unevenly distributed in the skin, spleen, and kidneys. The results obtained by the SBDC method are higher than the ideal values. The SBIC method restores the HbO_2 and Hb concentration estimates of the left skin, intestine and kidney, but the quantitative estimation error of the right organs is still large. In all profiles of HbO_2, Hb and sO_2, the $\mu_a^{estimated}$ reconstructed by our proposed method coincides with the μ_a^{ideal}. The SSE values between the ideal and estimated HbO_2, Hb and sO_2 images for all positions are listed in Table 1. For all images, our proposed method possesses the smallest value. The above results show that the HbO_2 and Hb concentrations of all organs have been restored to ideal values with our proposed method, as well as sO_2.

3.2. *Phantom experiment results*

We compared our proposed method and two other comparing methods in the tissue-mimicking phantom imaging experiment, and the results at 700 nm are shown in Fig. 5. The three rod-shaped inclusions of the phantom contained the same absorption material in the same concentration [Fig. 5(a)]. In the un-corrected PAT image, the signal of the inner rod is lower than that of the two outer rods due to laser attenuation [Fig. 5(a)]. The prior images of SBDC and SBIC methods are shown in Fig. 5(b). It is generated by manually segmenting the object contours from the PAT image. The LF distribution maps estimated using different methods are shown in Fig. 5(c). The ePAT images are shown in Fig. 5(d). The difference images between PAT and ePAT are shown in Fig. 5(e) and the reconstructed $\mu_a^{estimated}$ images are shown in Fig. 5(f). In the SBDC method, we choose 0.04 mm^{-1} as the μ_a value. In the SBIC method, the optimal μ_a value calculated by iteration is 0.01715 mm^{-1}.

At 700 nm, the μ_a value is relatively high in Chinese ink (0.12 mm^{-1}), moderate in Intralipid (0.006 mm^{-1}), and very small in water [Fig. 5(a)]. As expected, the LF map derived from our method shows that the LF does not change obviously in water, gradually decreases in the background containing Intralipid, and rapidly decays in the rod-shaped absorbers containing Chinese ink [Fig. 5(c)]. However, this feature has not been reflected in SBDC and SBIC methods. Similar to the un-corrected PAT image, the ePAT image derived from all three methods has an attenuated signal with increasing imaging depth [Fig. 5(d)]. However, the ePAT image derived from our method has a visually more similar attenuation variation to PAT: the signal intensity of the inner rod is lower than that of the two outer rods [Fig. 5(d)]. Further, it can be observed that the difference in SBDC and SBIC methods is larger than our proposed method, especially in regions with higher μ_a values (e.g., rod-shaped inclusions) [Fig. 5(e)]. In the reconstructed $\mu_a^{estimated}$ image obtained by our proposed method, the three rod-shaped absorbers have very similar pixel values, and for the same rod-shaped absorber, the pixel values become more homogeneous [Fig. 5(f)].

For further comparison, the image profiles of PAT, ePAT and $\mu_a^{estimated}$ are illustrated in Fig. 5(g, h), with the position along the white solid line in Fig. 5(a). The profiles show a high degree of overlap between the PAT and ePAT obtained by our proposed method, and the PAT signal of the two outer rod-shaped absorbers decreases with the increase of depth [Fig. 5(g)]. By contrast, there are large errors between the profiles of PAT and ePAT obtained by the SBDC and SBIC methods. The profile of the $\mu_a^{estimated}$ image obtained by our method shows that the μ_a values of these three rod-shaped inclusions have reached the same level, and the μ_a values of the two outer absorbers have become more homogeneous

Table 1
The SSE values between the ideal and estimated HbO_2, Hb and sO_2 images for all positions.

SSE	Methods		
	SBDC	SBIC	Proposed
HbO_2	180.351 ± 136.0068	17.2596 ± 35.3555	0.0028 ± 0.001
Hb	6.8366 ± 5.1225	1.1563 ± 2.4457	0.001 ± 0.0003
sO_2	10.6515 ± 8.7329	1.0628 ± 0.9624	0.0316 ± 0.0228

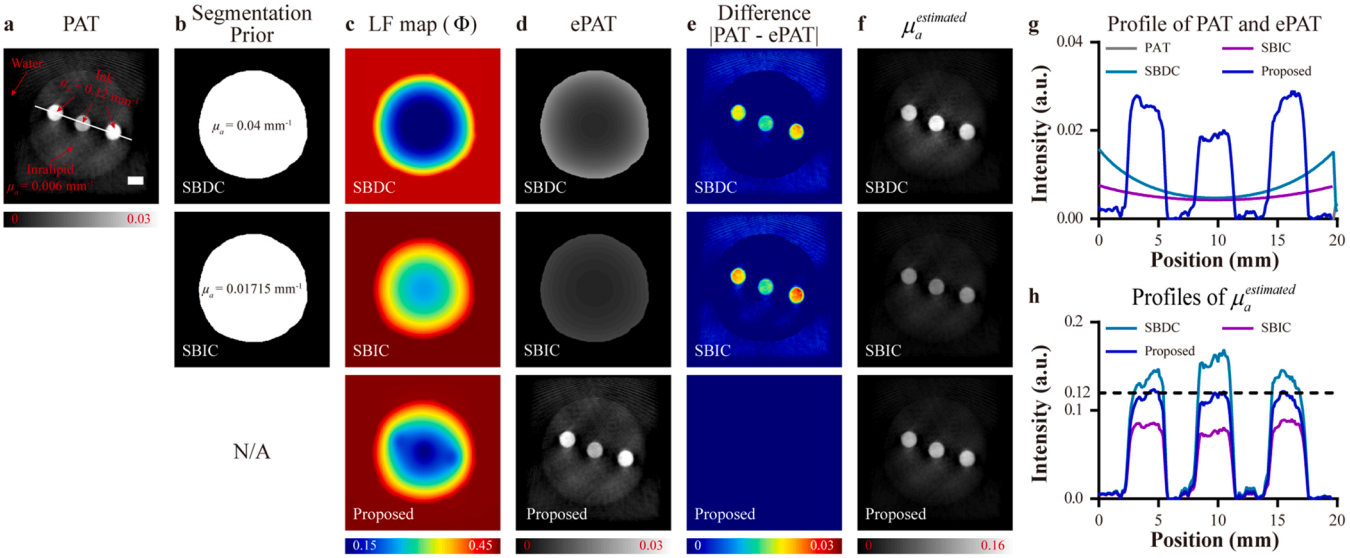

Fig. 5. Tissue-mimicking phantom experiment: (a) PAT: un-corrected PAT image. (b) Segmentation prior: segmentation results for SBDC and SBIC methods. (c) LF map (Φ): light fluence distribution maps estimated using different methods. (d) ePAT: estimated PAT images derived by using different methods. (e) Difference: the difference images between PAT and ePAT images. (f) $\mu_a^{estimated}$: μ_a images solved by different methods. (g) Profiles of PAT and ePAT images drawn along the white line in (a). (h) Profiles of $\mu_a^{estimated}$ images drawn along the white line in (a). Scale bar, 3 mm.

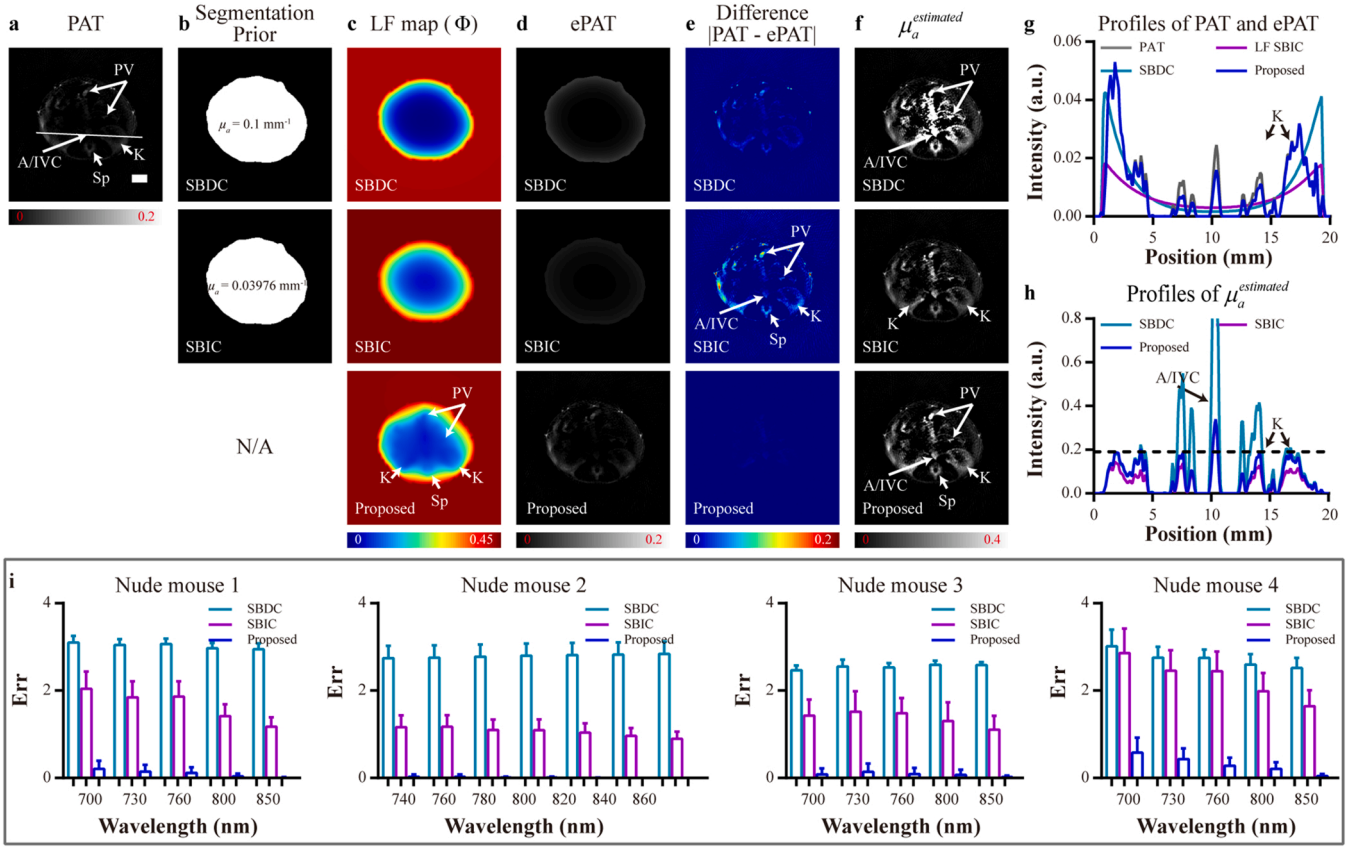

Fig. 6. In vivo animal experiment: (a) Un-corrected PAT image at the kidney position. (b) Segmentation prior: segmentation results for SBDC and SBIC methods. (c) LF map (Φ): light fluence distribution maps estimated using different methods. (d) ePAT: estimated PAT images derived by using different methods. (e) Difference: the difference images between PAT and ePAT images. (f) $\mu_a^{estimated}$: μ_a images solved by different methods. (g) Profiles of PAT and ePAT images drawn along the white line in (a). (h) Profiles of $\mu_a^{estimated}$ images drawn along the white line in (a). (i) The Err values between PAT and ePAT images for all nude mice at different wavelengths. Description of markers: A: artery; PV: portal vein; IVC: inferior vena cava; K: kidney; Sp: spine. Scale bar, 3 mm.

[Fig. 5(h)]. These results suggested that our method can reconstruct the real μ_a distribution in the tissue-mimicking phantom experiment.

3.3. Animal results

The results of the in vivo imaging of nude mice at 700 nm are shown in Fig. 6. Fig. 6(a) illustrates the PAT signal attenuation in the central features [artery, portal veins (PVs), inferior vena cava (IVC), the interior of the kidney and spine] due to the attenuation of the laser energy. The prior images of SBDC and SBIC methods generated by manually segmenting the object contours from the PAT image are shown in Fig. 6(b). The LF distribution maps estimated using different methods are shown in Fig. 6(c). The ePAT images are shown in Fig. 6(d) and the difference images between PAT and ePAT are shown in Fig. 6(e). The reconstructed $\mu_a^{estimated}$ images are shown in Fig. 6(f).

As can be seen from the results of SBDC and SBIC methods, the LF map and the ePAT image also have an attenuated signal with the increasing imaging depth [Fig. 6(c, d)]. However, this isotropic attenuation resulting from the uniform μ_a value makes the difference between PAT and ePAT very large [Fig. 6(e)]. The LF map estimated by our proposed method has a rapid decay in regions with higher μ_a values (kidneys, PV and spine), whereas the LF maps obtained by SBDC and SBIC methods attenuate isotropically [Fig. 6(c)]. The difference between PAT and ePAT obtained by our method is the smallest [Fig. 6(e)], which proves that one of the advantages of our method over SBDC and SBIC methods is that it can obtain a more accurate solution.

In the SBDC method, the accuracy of the results is depended on the manual choice of the μ_a value. For example, the $\mu_a^{estimated}$ image obtained by $\mu_a = 0.1\ mm^{-1}$ will cause excessive enhancement of central features (such as artery, IVC, and PVs) [Fig. 6(f)]. The $\mu_a^{estimated}$ image obtained by the SBIC method appears to be appropriate for the enhancement of the signal from deeper tissues ($\mu_a = 0.03976\ mm^{-1}$), but the signal within the same organ of the $\mu_a^{estimated}$ image is still inhomogeneous (e.g. kidney) [Fig. 6(f)]. The $\mu_a^{estimated}$ image obtained by our method effectively enhances the visibility of deep tissues, e.g., image intensity in the kidney has reached an even distribution [Fig. 6(f)].

To further assess the performance of these three methods, the image profiles of PAT, ePAT and $\mu_a^{estimated}$ at the position along the white solid line in Fig. 6(a) are illustrated in Fig. 6(g, h). The profiles show a high degree of overlap between the PAT and the ePAT image obtained by our proposed method [Fig. 6(g)]. By contrast, there are large errors between the profiles of PAT and ePAT obtained by the SBDC and SBIC methods. In the profile of the PAT image, the signals in the superficial layers of both the left and right kidneys are higher than those in deeper layers [Fig. 6(g), K arrow]. In the SBDC method, the signals of the deeper layers of the kidney are enhanced indiscriminately, resulting in much higher internal signals than external ones [Fig. 6(h), K arrow]. In the SBIC method, there is a small difference in the profile amplitudes within the left and right kidneys [Fig. 6(h), K arrow], which cannot be addressed by the setting of uniform μ_a value. In our proposed method, there is no obvious difference in the profile amplitudes within the left and right kidneys [Fig. 6(h)], and the signal amplitude of the central IVC is consistent with that of the SBIC method.

Furthermore, we measured the Err between the un-corrected PAT and ePAT images in the in vivo animal experiment of all four mice at different wavelengths, and the results are shown in Fig. 6(i). For the Err results, our proposed method is on average two orders of magnitude smaller than SBDC and SBIC methods at all wavelengths. Specifically, at 760 nm, the mean Err value of our proposed method for all animals is 0.091 ± 0.13, compared to 2.8906 ± 0.2711 for the SBDC method and 1.6342 ± 0.4762 for the SBIC method. This indicates that the ePAT image estimated by our method has reached a better approximation of the un-corrected PAT image.

Fig. 7(a-d) shows the HbO_2, Hb and sO_2 distribution images obtained from linear spectral unmixing. The HbO_2 of oxygen-rich (e.g., the artery) and Hb of hypoxic (the PV and IVC) blood vessels should be higher than in other tissues. However, these features are not reflected in the un-corrected images due to the laser energy attenuation [Fig. 7(a)]. This further leads to increased sO_2 value with increasing depth. The SBDC and SBIC methods enhance the concentrations of HbO_2 and Hb in the depth of the image [Fig. 7(b, c)]. However, due to the uniform μ_a value setting under different wavelengths in SBDC and SBIC methods, the sO_2 value still tends to increase with depth. There are still quantitative errors in the sO_2 values of the artery [Fig. 7(b, c)]. In the HbO_2 and Hb images obtained by our proposed method, all blood vessels are visible [Fig. 7(d)].

We have also calculated the difference images of HbO_2, Hb and sO_2 by using the un-corrected images as reference, and the results are shown in Fig. 7(e-g). As can be seen, the HbO_2 concentration in the artery and the Hb concentration in the veins (PV and IVC) have increased in the $\mu_a^{estimated}$ results. Nevertheless, the sO_2 value at the artery obtained by our

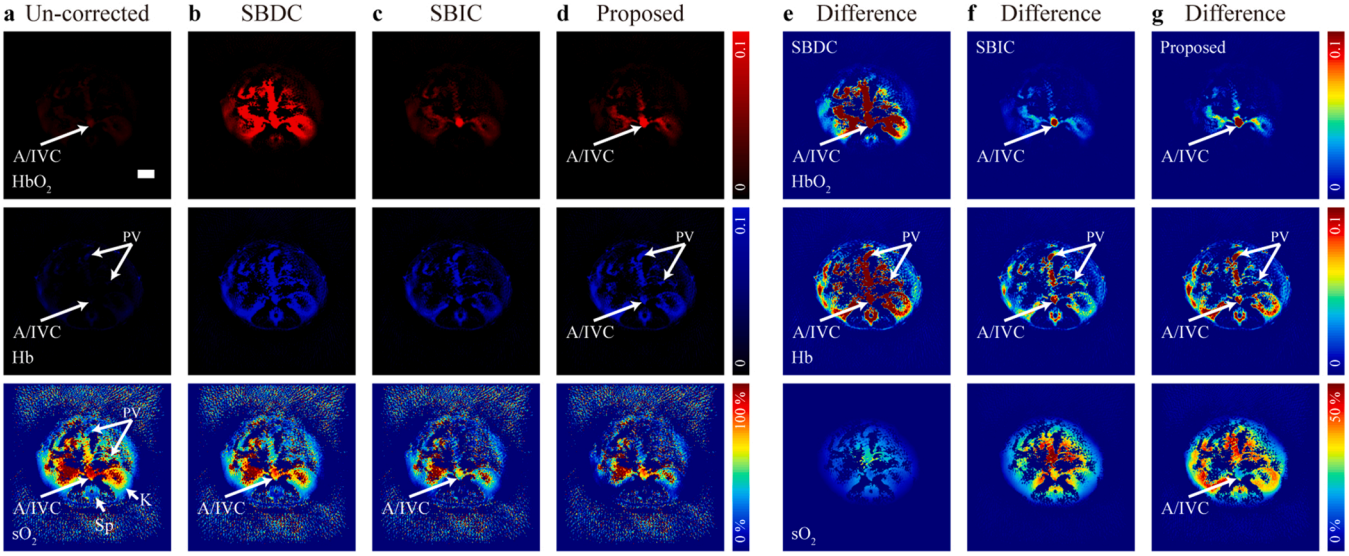

Fig. 7. Spectral un-mixing results of in vivo animal experiment: (a-d) The concentration distribution (HbO_2, Hb) and SO_2 images obtained by spectral un-mixing from un-corrected PAT and $\mu_a^{estimated}$ images. (e-g) The difference images of HbO_2, Hb and sO_2 by using un-corrected images as reference. Description of markers: A: artery; PV: portal vein; IVC: inferior vena cava; K: kidney; Sp: spine. Scale bar, 3 mm.

proposed method is still high, while the sO_2 value at the kidney and PV is significantly reduced. This indicates that our proposed method can obtain a more accurate endogenous absorber concentration distribution.

Finally, we applied these three methods to multispectral PAT images of the kidney region acquired from living nude mice after intravenous administration of 200 μl ICG (0.05 μg/μl). The spectrally un-mixed ICG images are shown in Fig. 8(a-d), and the difference images of ICG by using the un-corrected image as reference are shown in Fig. 8(e-g). the ICG is metabolized from the veins into the kidneys and spleen, and thus these positions should have high ICG signals. However, in the un-corrected spectral un-mixing results, the ICG concentration in the kidneys is not homogeneous (inside is lower than the outside), and the ICG signal of the IVC is very weak, which seriously affected the quantitative study of ICG metabolism [Fig. 8(a)]. The center concentration of ICG obtained by the SBDC method is over-enhanced [Fig. 8(b, e)], while the SBIC method has no significant improvement [Fig. 8(c, f)]. Both these two methods cannot restore the higher ICG concentration distribution in the spleen due to metabolism. The result derived from our proposed method shows that the visualization of deep ICG concentration, including the IVC, kidney and spleen, is enhanced [Fig. 8(d, g)]. These results indicate that our method can help obtain a more accurate exogenous probe distribution.

4. Discussions

The above results demonstrate that our method can directly reconstruct pixel-wise tissue μ_a maps and obtain the correct absorber distributions, revealing its attractive potential for the quantitative measurement of blood oxygenation and the concentration of various exogenous contrast agents. Our proposed method includes the following advantages:

Firstly, to ensure accuracy, our method converts the μ_a reconstruction problem to a nonlinear least square model, and proposes a two-step iterative optimization method to update the LF distribution and the μ_a map until convergence. This iterative algorithm allows optimizing both the LF map and the μ_a image simultaneously, and thus improves the convergence of the solution.

Secondly, previous methods such as SBDC and SBIC consider uniform μ_a distributions either on the whole body or within each organ. They do not match the real, spatially varying optical parameters in tissues. By contrast, our method directly solves this inhomogeneous μ_a map at pixel-level. By solving it in an iterative way, the obtained μ_a map is more accurate than region-wise methods, as proved by our experiments.

Thirdly, our proposed method is simple and does not require manual intervention. Both the SBDC and SBIC methods require segmentation of PAT images, and the SBDC method even requires manual assignment of optical parameters. Furthermore, the performance of the SBDC method is highly dependent on manually selected μ_a value, choosing a different μ_a value can lead to a deficient or excessive correction. Our method can automatically calculate the μ_a distribution without manual segmentation of the animal body or organs, thus largely simplifies the correction process and avoids the influence of subjective factors.

There are still some limitations in our study. Firstly, as in most previous studies [12,33,40,41], we assume that the reduced scattering coefficient is known because it is difficult to solve both the absorption and reduced scattering coefficients at the same time [32]. Secondly, we use a two-dimensional light transport model to estimate the LF distribution as in Ref [32]. However, in practice, the LF estimation should be carried out in three-dimension because PAT systems typically use diffuse illumination. Future work will require the design of the special objective functions for the 3D optical transport model for LF estimation, which in turn enables 3D μ_a reconstruction. Thirdly, our method requires a longer computation time while improving computational accuracy. The average computation time of our proposed method for a single-slice image is 92.49 s, so real-time imaging cannot be achieved. Finally, during image reconstruction, we set a uniform speed of sound distribution, but biological tissues are acoustically heterogeneous, therefore in our future work we also need to correct for the heterogeneous speed of sound.

5. Conclusions

In this paper, we developed a non-segmentation iterative method to directly reconstruct the μ_a images for quantitative PAT. Demonstrated in

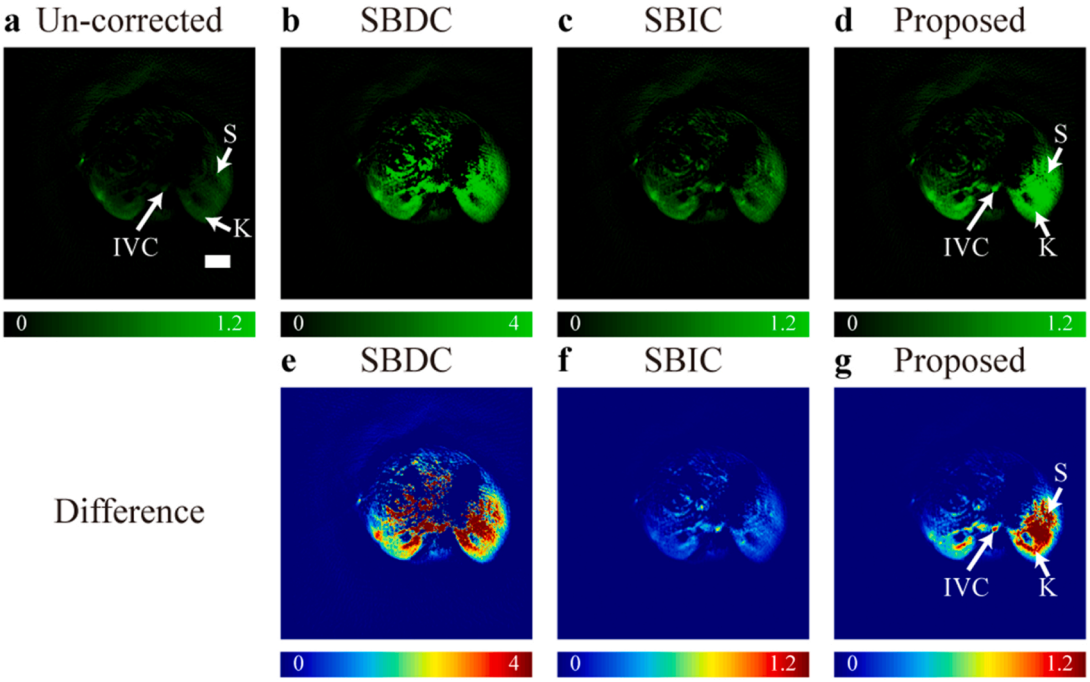

Fig. 8. ICG experiment: (a-d) The concentration distribution images of ICG obtained by spectral un-mixing. (e-g) The difference images by using the un-corrected image as reference. Description of markers: IVC: inferior vena cava; K: kidney; S: spleen. Scale bar, 3 mm.

the simulation experiments, phantom experiments and in vivo animal experiments, our method enables accurate reconstruction of spatially varying μ_a images at pixel-level. These findings provide a reliable foundation for the quantitative measurements of blood oxygenation and the various exogenous contrast agents, and therefore contribute to the advancement and future applications of the PAT technology.

CRediT authorship contribution statement

Shuangyang Zhang and Jiaming Liu: Methodology, Software, Investigation, Data Analysis, Writing - Original Draft **Zhichao Liang and Jia Ge**: Resources, Animal & Phantom Experiments **Yanqiu Feng, Wufan Chen, and Li Qi**: Conceptualization, Supervision, Funding acquisition, Writing - Review & Editing.

Declaration of Competing Interest

The authors declare that they have no known competing financial interests or personal relationships that could have appeared to influence the work reported in this paper.

Data availability

Data will be made available on request.

Acknowledgments

This work is supported in part by the Key-Area Research and Development Program of Guangdong Province 2018B030333001, in part by the Guangzhou Science and Technology Program 201804010375, in part by the Guangdong Provincial Natural Science Foundation 2021A1515012542 and 2022A1515011748, and in part by the Pearl River Talented Young Scholar Program 2017GC010282.

Appendix A. Supporting information

Supplementary data associated with this article can be found in the online version at doi:10.1016/j.pacs.2022.100390.

References

[1] L.V. Wang, J. Yao, A practical guide to photoacoustic tomography in the life sciences, Nat. Methods 13 (8) (2016) 627–638.
[2] L.V. Wang, S. Hu, Photoacoustic tomography: in vivo imaging from organelles to organs, Science 335 (6075) (2012) 1458–1462.
[3] L. Nie, X. Chen, Structural and functional photoacoustic molecular tomography aided by emerging contrast agents, Chem. Soc. Rev. 43 (20) (2014) 7132–7170.
[4] S. Zhang, L. Qi, X. Li, J. Liu, S. Huang, J. Wu, R. Liu, Y. Feng, Q. Feng, W. Chen, Photoacoustic imaging of living mice enhanced with a low-cost contrast agent, Biomed. Opt. Express 10 (11) (2019) 5744–5754.
[5] S. Tzoumas, N. Deliolanis, S. Morscher, V. Ntziachristos, Unmixing molecular agents from absorbing tissue in multispectral optoacoustic tomography, IEEE Trans. Med Imaging 33 (1) (2014) 48–60.
[6] S. Zackrisson, S. van de Ven, S.S. Gambhir, Light in and sound out: emerging translational strategies for photoacoustic imaging, Cancer Res. 74 (4) (2014) 979–1004.
[7] I. Stoffels, S. Morscher, I. Helfrich, U. Hillen, J. Leyh, N.C. Burton, T.C. Sardella, J. Claussen, T.D. Poeppel, H.S. Bachmann, A. Roesch, K. Griewank, D. Schadendorf, M. Gunzer, J. Klode, Metastatic status of sentinel lymph nodes in melanoma determined noninvasively with multispectral optoacoustic imaging, Sci. Transl. Med. 7 (317) (2015), 317ra199.
[8] F. Knieling, C. Neufert, A. Hartmann, J. Claussen, A. Urich, C. Egger, M. Vetter, S. Fischer, L. Pfeifer, A. Hagel, C. Kielisch, R.S. Gortz, D. Wildner, M. Engel, J. Rother, W. Uter, J. Siebler, R. Atreya, W. Rascher, D. Strobel, M.F. Neurath, M. J. Waldner, Multispectral optoacoustic tomography for assessment of Crohn's disease activity, N. Engl. J. Med. 376 (13) (2017) 1292–1294.
[9] L. Lin, P. Hu, J. Shi, C.M. Appleton, K. Maslov, L. Li, R. Zhang, L.V. Wang, Single-breath-hold photoacoustic computed tomography of the breast, Nat. Commun. 9 (1) (2018) 2352.
[10] I. Ivankovic, E. Mercep, C.G. Schmedt, X.L. Deán-Ben, D. Razansky, Real-time volumetric assessment of the human carotid artery: handheld multispectral optoacoustic tomography, Radiology 291 (1) (2019) 45–50.
[11] B. Cox, J.G. Laufer, S.R. Arridge, P.C. Beard, Quantitative spectroscopic photoacoustic imaging: a review, J. Biomed. Opt. 17 (6) (2012), 061202.
[12] B.T. Cox, S.R. Arridge, K.P. Kostli, P.C. Beard, Two-dimensional quantitative photoacoustic image reconstruction of absorption distributions in scattering media by use of a simple iterative method, Appl. Opt. 45 (8) (2006) 1866–1875.
[13] Z. Guo, S. Hu, L.V. Wang, Calibration-free absolute quantification of optical absorption coefficients using acoustic spectra in 3D photoacoustic microscopy of biological tissue, Opt. Lett. 35 (12) (2010) 2067–2069.
[14] Z. Guo, C. Favazza, A. Garcia-Uribe, L.V. Wang, Quantitative photoacoustic microscopy of optical absorption coefficients from acoustic spectra in the optical diffusive regime, J. Biomed. Opt. 17 (6) (2012), 066011.
[15] J. Yao, L. Wang, J.M. Yang, K.I. Maslov, T.T. Wong, L. Li, C.H. Huang, J. Zou, L. V. Wang, High-speed label-free functional photoacoustic microscopy of mouse brain in action, Nat. Methods 12 (5) (2015) 407–410.
[16] T. Saratoon, T. Tarvainen, B.T. Cox, S.R. Arridge, A gradient-based method for quantitative photoacoustic tomography using the radiative transfer equation, Inverse Probl. 29 (7) (2013).
[17] L. Yao, Y. Sun, H. Jiang, Quantitative photoacoustic tomography based on the radiative transfer equation, Opt. Lett. 34 (12) (2009) 1765–1767.
[18] S. Zhang, L. Qi, X. Li, Z. Liang, X. Sun, J. Liu, L. Lu, Y. Feng, W. Chen, M.R. I. Information-Based, Correction and restoration of photoacoustic tomography, IEEE Trans. Med Imaging PP (2022).
[19] M.A. Mastanduno, S.S. Gambhir, Quantitative photoacoustic image reconstruction improves accuracy in deep tissue structures, Biomed. Opt. Express 7 (10) (2016) 3811–3825.
[20] R. Hochuli, S. Powell, S. Arridge, B. Cox, Quantitative photoacoustic tomography using forward and adjoint Monte Carlo models of radiance, J. Biomed. Opt. 21 (12) (2016).
[21] J. Buchmann, B. Kaplan, S. Powell, S. Prohaska, J. Laufer, Three-dimensional quantitative photoacoustic tomography using an adjoint radiance Monte Carlo model and gradient descent, J. Biomed. Opt. 24 (6) (2019) 1–13.
[22] A.Q. Bauer, R.E. Nothdurft, T.N. Erpelding, L.V. Wang, J.P. Culver, Quantitative photoacoustic imaging: correcting for heterogeneous light fluence distributions using diffuse optical tomography, J. Biomed. Opt. 16 (9) (2011), 096016.
[23] A. Hussain, E. Hondebrink, J. Staley, W. Steenbergen, Photoacoustic and acousto-optic tomography for quantitative and functional imaging, Optica 5 (12) (2018) 1579–1589.
[24] A. Pattyn, Z. Mumm, N. Alijabbari, N. Duric, M.A. Anastasio, M. Mehrmohammadi, Model-based optical and acoustical compensation for photoacoustic tomography of heterogeneous mediums, Photoacoustics 23 (2021).
[25] B. Banerjee, S. Bagchi, R.M. Vasu, D. Roy, Quantitative photoacoustic tomography from boundary pressure measurements: noniterative recovery of optical absorption coefficient from the reconstructed absorbed energy map, J. Opt. Soc. Am. A Opt. Image Sci. Vis. 25 (9) (2008) 2347–2356.
[26] Z. Yuan, Q. Wang, H. Jiang, Reconstruction of optical absorption coefficient maps of heterogeneous media by photoacoustic tomography coupled with diffusion equation based regularized Newton method, Opt. Express 15 (26) (2007) 18076–18081.
[27] A.A. Oraevsky, B.T. Cox, L.V. Wang, S.R. Arridge, P.C. Beard, Gradient-based quantitative photoacoustic image reconstruction for molecular imaging, Photons Plus Ultrasound: Imaging and Sensing 2007: The Eighth Conference on Biomedical Thermoacoustics, Optoacoustics, and Acousto-optics, 2007.
[28] B.T. Cox, S.R. Arridge, P.C. Beard, Estimating chromophore distributions from multiwavelength photoacoustic images, J. Opt. Soc. Am. A Opt. Image Sci. Vis. 26 (2) (2009) 443–455.
[29] J. Buchmann, B. Kaplan, S. Powell, S. Prohaska, J. Laufer, Quantitative PA tomography of high resolution 3-D images: experimental validation in a tissue phantom, Photoacoustics 17 (2020), 100157.
[30] S. Mandal, X.L. Deán-Ben, D. Razansky, Visual quality enhancement in optoacoustic tomography using active contour segmentation priors, IEEE Trans. Med. Imaging 35 (10) (2016) 2209–2217.
[31] Z. Liang, S. Zhang, J. Wu, X. Li, Z. Zhuang, Q. Feng, W. Chen, L. Qi, Automatic 3-D segmentation and volumetric light fluence correction for photoacoustic tomography based on optimal 3-D graph search, Med. Image Anal. 75 (2022), 102275.
[32] F.M. Brochu, J. Brunker, J. Joseph, M.R. Tomaszewski, S. Morscher, S.E. Bohndiek, Towards quantitative evaluation of tissue absorption coefficients using light fluence correction in optoacoustic tomography, IEEE Trans. Med. Imaging 36 (1) (2017) 322–331.
[33] S. Zhang, L. Qi, X. Li, Z. Liang, J. Wu, S. Huang, J. Liu, Z. Zhuang, Y. Feng, Q. Feng, W. Chen, In vivo co-registered hybrid-contrast imaging by successive photoacoustic tomography and magnetic resonance imaging, bioRxiv (2021).
[34] T. Tarvainen, B.T. Cox, J.P. Kaipio, S.R. Arridge, Reconstructing absorption and scattering distributions in quantitative photoacoustic tomography, Inverse Probl. 28 (8) (2012).
[35] X. Li, L. Qi, S.Y. Zhang, S.X. Huang, J. Wu, L.J. Lu, Y.Q. Feng, Q.J. Feng, W.F. Chen, Model-based optoacoustic tomography image reconstruction with non-local and sparsity regularizations, IEEE Access 7 (2019) 102136–102148.
[36] X. Li, S. Zhang, J. Wu, S. Huang, Q. Feng, L. Qi, W. Chen, Multispectral interlaced sparse sampling photoacoustic tomography, IEEE Trans. Med. Imaging 39 (11) (2020) 3463–3474.
[37] L. Qi, S. Huang, X. Li, S. Zhang, L. Lu, Q. Feng, W. Chen, Cross-sectional photoacoustic tomography image reconstruction with a multi-curve integration model, Comput. Methods Prog. Biomed. 197 (2020), 105731.

[38] L. Qi, J. Wu, X. Li, S. Zhang, S. Huang, Q. Feng, W. Chen, Photoacoustic tomography image restoration with measured spatially variant point spread functions, IEEE Trans. Med. Imaging 40 (9) (2021) 2318–2328.
[39] X. Li, J. Ge, S. Zhang, J. Wu, L. Qi, W. Chen, Multispectral interlaced sparse sampling photoacoustic tomography based on directional total variation, Comput. Methods Prog. Biomed. 214 (2022), 106562.
[40] T. Jetzfellner, D. Razansky, A. Rosenthal, R. Schulz, K.H. Englmeier, V. Ntziachristos, Performance of iterative optoacoustic tomography with experimental data, Appl. Phys. Lett. 95 (1) (2009).
[41] J. Li, C. Wang, T.T. Chen, T. Lu, S. Li, B.A. Sun, F. Gao, V. Ntziachristos, Deep learning-based quantitative optoacoustic tomography of deep tissues in the absence of labeled experimental data, Optica 9 (1) (2022) 32–41.
[42] M. Schweiger, S. Arridge, The Toast++ software suite for forward and inverse modeling in optical tomography, J. Biomed. Opt. 19 (4) (2014), 040801.
[43] N. Keshava, J.F. Mustard, Spectral unmixing, IEEE Signal Process. Mag. 19 (1) (2002) 44–57.
[44] Y. Zhang, L. Wang, Video-rate ring-array ultrasound and photoacoustic tomography, IEEE Trans. Med. Imaging 39 (12) (2020) 4369–4375.
[45] G. Alexandrakis, F.R. Rannou, A.F. Chatziioannou, Tomographic bioluminescence imaging by use of a combined optical-PET (OPET) system: a computer simulation feasibility study, Phys. Med. Biol. 50 (17) (2005) 4225–4241.
[46] R. Cubeddu, A. Pifferi, P. Taroni, A. Torricelli, G. Valentini, A solid tissue phantom for photon migration studies, Phys. Med. Biol. 42 (10) (1997) 1971–1979.

Shuangyang Zhang received his B. Eng. degree in 2017 from Southern Medical University. He is currently pursuing a Ph.D. degree in Engineering at the School of Biomedical Engineering, Southern Medical University. His research interests include multimodal image registration and information fusion.

Jiaming Liu received her B. Eng. degree in 2017 from Southern Medical University, Guangzhou, China. She is currently pursuing a Ph.D. degree in Engineering at Southern Medical University, China. Her research focuses on small animal functional MRI.

Zhichao Liang received his bachelor's degree from Southern Medical University in 2021. He is currently pursuing the master's degree in the school of Biomedical Engineering, Southern Medical University. His research interests include photoacoustic tomography and image segmentation.

Jia Ge is currently pursuing a master's degree in engineering at the School of Biomedical Engineering, Southern Medical University. His research interest covers multispectral photoacoustic tomography.

Yanqiu Feng received his Ph.D. degree in Biomedical Engineering from Southern Medical University in 2005. He is currently a full professor at the Guangdong Provincial Key Laboratory of Medial Image Processing, School of Biomedical Engineering, Southern Medical University. His research interests include biomedical image processing and quantitative MRI imaging.

Wufan Chen received his B.S. degree in 1975 and M.Sc. degree in 1981, both from Beihang University. He is currently a full professor at the Guangdong Provincial Key Laboratory of Medial Image Processing, School of Biomedical Engineering, Southern Medical University. His research interests include biomedical imaging principle and image processing.

Li Qi received his Ph.D. degree in Optical Engineering in 2016 from Nanjing University. He is currently a lecturer at the Guangdong Provincial Key Laboratory of Medial Image Processing, School of Biomedical Engineering, Southern Medical University in Guangzhou, China. His research interests include photoacoustic imaging and optical coherence tomography.